Dynamic Nuclear Polarization of Silicon Carbide Micro- and Nanoparticles

Lin, Min; Breukels, Vincent; Scheenen, Tom W. J.; Paulusse, Jos M. J.

Published in:
ACS Applied Materials & Interfaces

DOI:
10.1021/acsami.1c07156

Publication date:
2021

ACS APPLIED MATERIALS & INTERFACES

www.acsami.org

Research Article

Dynamic Nuclear Polarization of Silicon Carbide Micro- and Nanoparticles

Min Lin, Vincent Breukels, Tom W. J. Scheenen,* and Jos M. J. Paulusse*

Cite This: *ACS Appl. Mater. Interfaces* 2021, 13, 30835−30843

Read Online

ACCESS | Metrics & More | Article Recommendations | Supporting Information

ABSTRACT: Two dominant crystalline phases of silicon carbide (SiC): α-SiC and β-SiC, differing in size and chemical composition, were investigated regarding their potential for dynamic nuclear polarization (DNP). ^{29}Si nuclei in α-SiC micro- and nanoparticles with sizes ranging from 650 nm to 2.2 μm and minimal oxidation were successfully hyperpolarized without the use of free radicals, while β-SiC samples did not display appreciable degrees of polarization under the same polarization conditions. Long T_1 relaxation times in α-SiC of up to 1600 s (~27 min) were recorded for the ^{29}Si nuclei after 1 h of polarization at a temperature of 4 K. Interestingly, these promising α-SiC particles allowed for direct hyperpolarization of both ^{29}Si and ^{13}C nuclei, resulting in comparably strong signal amplifications. Moreover, the T_1 relaxation time of ^{13}C nuclei in 750 nm-sized α-SiC particles was over 33 min, which far exceeds T_1 times of conventional ^{13}C DNP probes with values in the order of 1−2 min. The present work demonstrates the feasibility of DNP on SiC micro- and nanoparticles and highlights their potential as hyperpolarized magnetic resonance imaging agents.

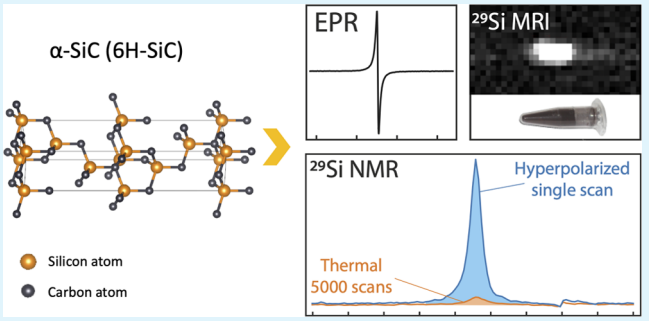

KEYWORDS: *silicon carbide, hyperpolarization, dynamic nuclear polarization, spin-lattice relaxation, nanoparticles*

INTRODUCTION

Magnetic resonance imaging (MRI) is a noninvasive, radiation-free diagnostic imaging tool giving exquisite soft tissue contrast and high anatomical resolution. However, its application in molecular imaging has often been restricted due to its inherently low sensitivity.[1,2] Conventional MRI modalities usually detect high natural abundance nuclei, such as the protons in water or lipid molecules, to obtain sufficient signal intensity in spite of the low degree of polarization under thermal equilibrium.[3] Contrast agents are frequently used to improve measurement sensitivities by shortening T_1 or T_2 relaxation times of water protons in close contact or proximity to the agent.[4,5] However, accumulation of gadolinium-based contrast agents after (repeated) administration gives concerns regarding toxicity issues.[6,7] A different approach is to perform imaging of the contrast agent or labeled particle itself instead of its effect on water protons, and use the high proton signal of water as an anatomical reference. Particles containing different nuclei can be observed without issues regarding the high proton background signal of water, and in principle, any nucleus with a nonzero net spin number, such as ^{13}C, ^{15}N, ^{19}F, ^{29}Si, or ^{31}P, can be imaged with MRI.[8−10] Unfortunately, direct detection of nuclei other than protons remains difficult due to low gyromagnetic ratios, low natural abundancies, and low concentrations of particles of interest, leading to long acquisition times and low spatial resolutions.

An interesting alternative strategy that alleviates the sensitivity problem of MRI is hyperpolarization of the spins of interest, which increases nuclear spin polarization far beyond thermal equilibrium.[11] Dynamic nuclear polarization (DNP) is a technique that utilizes the much higher spin polarization of unpaired electrons to hyperpolarize nearby nuclear spin elements by transferring the electron polarization under microwave irradiation. The most widespread DNP method in MRI is dissolution DNP, which results in up to 10 000-fold signal amplification compared to typical thermal polarization.[1] Dissolution DNP has been used to investigate metabolic pathways and to study enzymatic activities. Small hyperpolarized ^{13}C-labeled substrates, such as 1-^{13}C-pyruvic acid or 1-^{13}C-fumarate, have been successfully used to detect aberrant metabolism in cell suspensions, animal models, and human tumors.[12−15] However, the hyperpolarized state is relatively short-lived, and the polarization will restore to thermal equilibrium with the relaxation time constant T_1. The majority of hyperpolarized ^{13}C-labeled molecules have a T_1 in the order

Received: April 19, 2021
Accepted: June 13, 2021
Published: June 25, 2021

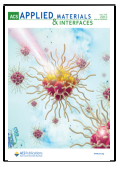

of 1 min or less.[16] Therefore, when used as tracers or substrates, imaging is restricted to visualizing fast biological processes in areas or organs that can easily be reached by the tracer. Slower biological processes, such as protein-cell binding, tracer diffusion, and metabolism in tissues, cannot be studied. Moreover, these short lifetimes cause significant signal decay during quality control of the hyperpolarized substances, intravenous administration, and transport to the tissue of interest, impeding general application in the clinic.

^{13}C or ^{29}Si nuclei in diamond and silicon particles have been demonstrated to display remarkably long T_1 relaxation times of up to several hours[17−21] and alleviate the short-lifetime issues associated with ^{13}C-labeled small molecules. Since interactions between nearby spin elements result in relaxation, spatial isolation of spin elements beyond the distance of spin interaction in a solid matrix can impede relaxation processes, leading to dramatically increased T_1 times. For instance, diamonds have been shown to display spin-lattice relaxation times of as long as 3−4 h.[17] ^{13}C nuclei in micro/nanosized diamonds have been successfully hyperpolarized, showing enhanced DNP signals. However, T_1 times in nanodiamonds with particle sizes ranging from 30 to 500 nm are still relatively short, usually in the order of 5 min or less,[22] though these particle sizes are most interesting for biomedical applications.

Aptekar and Cassidy et al. elegantly demonstrated extended T_1 relaxation times of up to 5 h for hyperpolarized ^{29}Si nuclei in silicon microparticles.[19,23] Interestingly, the presence of unpaired electrons in surface defects allows for hyperpolarization without the addition of exogenous radicals.[24,25] Whiting et al. employed hyperpolarized silicon particles with sizes ranging from 20 nm to 2 μm in the visualization of tumorous tissue.[26] Their investigations revealed a size dependence for the recorded T_1 relaxation times, with larger particle sizes tending to display longer T_1 times and stronger DNP enhancements.[27,28] However, the relatively large size and limited solubility of these silicon particles impede studies involving blood circulation.[29]

In recent years, silicon carbide (SiC) received increased attention as a viable material in biomedicine (e.g., in device fabrication, for implants, coatings, and scaffolds) due to its high biocompatibility and low toxicity.[30] SiC may however also have potential for use in hyperpolarization MRI. The divacancy defects in SiC, much like the diamond nitrogen-vacancy center, can be polarized through optically pumped dynamic nuclear polarization.[31,32] Studies by Hartman et al. demonstrate long ^{29}Si and ^{13}C T_1 relaxation times of up to 7 h for high-purity bulk silicon carbide.[33] Importantly, the Larmor frequencies of ^{29}Si and especially ^{13}C are both within the tuning ranges of commercial multinuclear MRI systems, building on existing imaging infrastructure. SiC therefore presents an interesting, yet hardly explored material for sensitivity-enhanced MRI.

In this work, we study the potential of various SiC samples with different crystal structures (α-SiC and β-SiC), sizes (micro- and nanoparticles), and surface groups for DNP, to evaluate the feasibility of SiC as hyperpolarized MRI agents.

MATERIALS AND METHODS

Silicon carbide (SiC) with two different crystalline phases, β-SiC and α-SiC, were obtained from four commercial sources. All information below about SiC, such as (average) particle sizes, color, and preparation methods are according to supplier specifications. β-SiC with particle size ranging from 100 to 1200 nm (β-$SiC_{100-1200,ST}$, gray powder) and α-SiC with particle size ranging from 200 to 1200 nm (α-$SiC_{200-1200,ST}$, light gray powder) were purchased from STREM Chemicals, Inc. β-SiC samples with average particle sizes (APS) of 18 nm (β-$SiC_{18,US}$, gray powder) and 80 nm (β-$SiC_{80,US}$, gray powder), as well as one α-SiC with APS of 800 nm (α-$SiC_{800,US}$, light gray powder) were purchased from US Research Nanomaterials, Inc. β-$SiC_{18,US}$ and β-$SiC_{80,US}$ were prepared by laser synthesis and plasma chemical vapor deposition (CVD), respectively. α-SiC with a size range of 5−250 nm (α-$SiC_{5-250,PC}$), prepared via a hot plasma jet process, was purchased from PlasmaChem. α-SiC samples with APS of 650 nm (α-$SiC_{650,Ab}$), 750 nm (α-$SiC_{750,Ab}$), and 2.2 μm (α-$SiC_{2200,Ab}$), prepared via the Acheson process, followed by ball milling, were purchased from ABCR GmbH (Germany). Purities of all SiC samples were >99%; no further purification was carried out on the samples unless stated otherwise. Table S1 summarizes the primary information of all samples provided by the manufacturer, and information about crystalline phase as determined here.

X-ray diffraction measurements were used to determine the lattice parameters of the investigated SiC samples. SiC powder samples were characterized by X-ray diffraction (XRD) on a PANalytical Philips X'Pert MPD diffractometer at room temperature using Cu Kα.

Scanning electron microscopy (SEM) images were recorded on a Zeiss Merlin HR-SEM spectrometer. Dilute suspensions of SiC powder in water were sonicated for 30 min, after which a droplet of the suspension was placed onto a silicon platform. Particle size distributions were determined with ImageJ.

Attenuated total reflectance (ATR)−FT-IR spectroscopy (Bruker Alpha) was used to analyze the surface groups of SiC samples.

Continuous-wave electron paramagnetic resonance (EPR) spectra were recorded at room temperature using an X-band EMX spectrometer (Bruker Biospin GmbH, Germany). The magnetic field was swept from 3100 to 3600 Gauss with 1024 points, at a modulation frequency of 100 kHz, 60 ms conversion time, and 164 ms time constant. The g-value was determined from the zero-crossing in the spectrum. Samples sizes between 0.5 and 2.0 mg were loaded into a glass capillary (OD = 780 μm), closed off with wax. This sample was placed inside the EPR tube. Using these small sizes resulted in minimum retuning between samples and comparable Q-factors, allowing semiquantitative evaluation of the electron density.

Dynamic nuclear polarization (DNP) was performed on a 3.38 T in-house-built polarizer, comprising a pumped bath cryostat,[34] an iSpin NMR spectrometer (Spincore Technologies, Florida), and a 94−96 GHz microwave source (Virginia Diodes, Inc., Virginia). A fixed ^{29}Si or ^{13}C tuned Alderman−Grant coil made to fit the sample was inductively coupled to an un-tuned saddle coil connected to the spectrometer. For ^{29}Si DNP measurements, about 60 mg of sample powder was tightly packed and enclosed in a poly(tetrafluoroethylene) (PTFE) cup. Microwave irradiation with frequency modulation was performed with a triangular-shaped modulation from 94.6500 to 94.7375 GHz, with a modulation frequency of 500 Hz. Spectra were processed using the ssNake software package,[35] using a 500 Hz line broadening prior to Fourier transform. DNP buildup curves were recorded with a series of pulse-acquire experiments with a repetition time (TR) of 60 s and a low flip angle of ~15°. The DNP enhancement value of ^{29}Si in the solid state was obtained by comparing the integrated signal intensity of the hyperpolarized sample with the thermal equilibrium signal. Thermal polarization was measured using the same setup as used for DNP experiments.

Magnetic resonance imaging and T_1 relaxation measurements were performed on an 11.7 T Bruker BioSpec MRI system using an in-house built three turn solenoid coil tuned to ^{29}Si (~99.3 MHz). After polarization in the DNP setup, samples were taken out and transferred as a solid into the scanner. T_1 measurements were recorded using a pulse-acquire scheme with a TR of 60 or 120 s and flip angle of approximately 18°. Imaging was performed using a single-shot multiecho RARE (rapid acquisition with relaxation enhancement) sequence with 8 (sagittal) complete images recorded using a single 90° excitation with multiple refocusing. The single-slice images (10 mm thickness) existed of 32 × 32 pixels over a field of view of 64 × 64 mm^2. With an echo spacing of 2.02 ms and a RARE factor of 32, every

https://doi.org/10.1021/acsami.1c07156
ACS Appl. Mater. Interfaces 2021, 13, 30835−30843

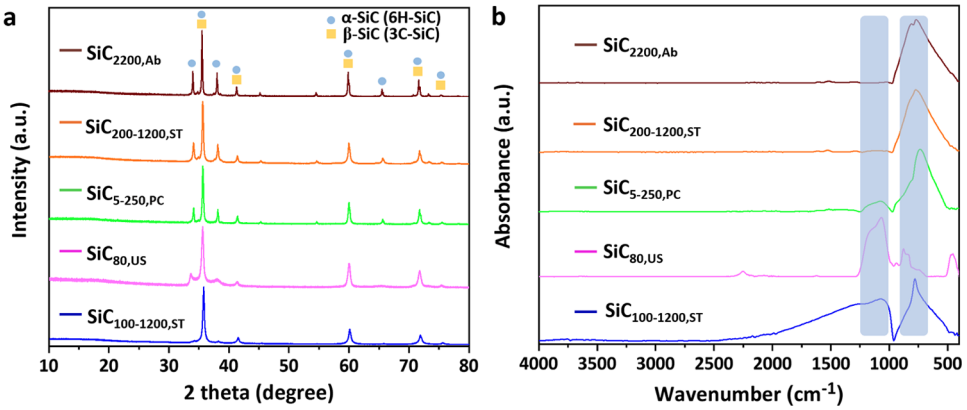

Figure 1. SiC characterization: (a) XRD and (b) FT-IR spectra of representative SiC samples.

64.5 ms a complete image was acquired, repeated 8 times resulting in spin echo images at 2.02, 66.5, 131.1, 195.7, 260.2, 324.8, 389.3, and 453.9 ms. With this single-shot acquisition, all hyperpolarized magnetization was used at once.

RESULTS AND DISCUSSION

Characterization of SiC. Particle size, crystal phase, and surface groups of SiC may affect DNP enhancement and T_1 relaxation time. All tested SiC samples were therefore characterized in detail to confirm the manufacturer-provided properties. XRD was carried out first to confirm the crystal phase of the SiC samples, since crystal structure and defects form a source of electrons that can be used for DNP. Figure 1a shows the XRD patterns of five representative SiC samples. The bottom curve (blue) shows diffraction peaks at 35.6, 41.5, 59.8, 71.8, and 75.4°, which could, respectively, be indexed as the (111), (200), (220), (311), and (222) reflections and well match with a β-SiC phase.[36,37] This sample has a cubic crystal structure and 3C-SiC is the only cubic polytype. The pink curve ($SiC_{80,US}$) exhibits an additional weak diffraction peak at 34.1°, usually indicating stacking faults within the crystals.[38] The remaining samples (Figure 1a, green, orange, and red curve) feature diffraction peaks at 34.1, 41.5, and 65.5° that are in agreement with an α-SiC phase.[39] XRD results of the α-SiC samples are consistent with the 6H-SiC polytype; however, other possible polytypes such as 4H-SiC may also exist.[40] Notably, α-SiC can consist of many different polytypes due to the different stacking sequences of carbon and silicon atoms in its crystal structure. XRD alone is not enough to distinguish all possible polytypes in SiC samples, further characterization, for example by low-temperature photoluminescence (LTPL) can help to understand the structure of SiC in more detail.[41] At present, XRD measurements mainly display the differences of crystal phase in these SiC samples. Therefore, the five samples are assigned as β-$SiC_{100-1200,ST}$, β-$SiC_{80,US}$, α-$SiC_{5-250,PC}$, α-$SiC_{200-1200,ST}$, and α-$SiC_{2200,Ab}$, according to their dominant crystal phases, as well as their particle sizes as provided by the suppliers. Detailed sample information can be found in Figure S1 and Table S1.

SiC samples were further studied using FT-IR spectroscopy to determine the nature of their surface functionality, which may affect hyperpolarization buildup and relaxation times. All β-SiC samples, such as β-$SiC_{18,US}$, β-$SiC_{80,US}$, and β-$SiC_{100-1200,ST}$ (Figures 1b and S2a), display two intense absorption peaks at 1076 and 785 cm^{-1}, indicating Si−O−Si bonds (1076 and 467 cm^{-1}) and Si−C stretching vibrations.[42,43] For α-SiC samples, only α-$SiC_{5-250,PC}$ shows both significant Si−O−Si and Si−C absorption peaks. The remaining α-SiC samples primarily reveal intense Si−C bonds (770 cm^{-1}) and only contain a very weak Si−O−Si band at about 1100 cm^{-1} (Figure 1b, orange and red curves; Figure S2, pink curve), indicating there are no significant silicon oxide contributions in these α-SiC samples. In addition, the SiC samples are very stable over time, as IR spectroscopy remains unaltered even after 2 years of storage without exposure to air (Figure S2b).

Finally, the particle size distribution of each sample as provided by the suppliers was assessed by scanning electron microscopy (SEM) imaging (representative samples in Figure 2). According to the size provided by the suppliers, sample α-$SiC_{5-250,PC}$ with a size ranging from 5 to 250 nm has a mean size of 133 nm. The mean sizes of α-$SiC_{650,Ab}$ (Figure 2b) and α-$SiC_{2200,Ab}$ (Figure 2d) are found to be 712 nm and 3.6 μm, respectively. The mean size of sample α-$SiC_{800,US}$ (Figure 2b) is 921 nm and SEM images of other SiC samples are shown in Figure S3. The particle sizes of these samples, as determined by SEM, are not fully consistent with the sizes provided by the suppliers, and we therefore primarily consider size trends, rather than precise particle sizes for the following studies. The morphology of SiC nanoparticles in samples β-$SiC_{18,US}$ and β-$SiC_{80,US}$ is spherical. In sample α-$SiC_{5-250,PC}$ a mixture of differently shaped particles is observed, such as cubic, hexagonal, as well as spherical, presumably due to the hot plasma jet synthesis process. The observed morphologies of other submicron and micron-sized SiC particles are irregularly shaped fragments (Figure 2).

EPR Analysis of SiC. The concentration of defects in the SiC particles determines the number of free electrons that can be directly hyperpolarized. EPR was performed to determine the nature and density of these defects and to obtain the microwave frequency for maximum polarization transfer. Figure 3a shows semiquantitative EPR spectra of selected SiC samples. Interestingly, the densities of free electrons are higher in α-SiC than in β-SiC samples. Notably, the similarly sized samples α-$SiC_{200-1200,ST}$ and β-$SiC_{100-1200,ST}$, which only differ in crystal phase, displays a ~2.5-fold difference in free electron density. The g-values of α-$SiC_{200-1200,ST}$ and β-$SiC_{100-1200,ST}$ are 2.0024 and 2.0025, respectively, which are typical of C-related defects (carbon vacancies).[44,45] It is worth mentioning that a different surface composition, such as a silicon oxide layer, may result in decreased densities of free electrons. For example, FT-IR analysis on sample α-$SiC_{5-250,PC}$ reveals strong contributions by Si−O−Si bonds (see Figure

https://doi.org/10.1021/acsami.1c07156
ACS Appl. Mater. Interfaces 2021, 13, 30835−30843

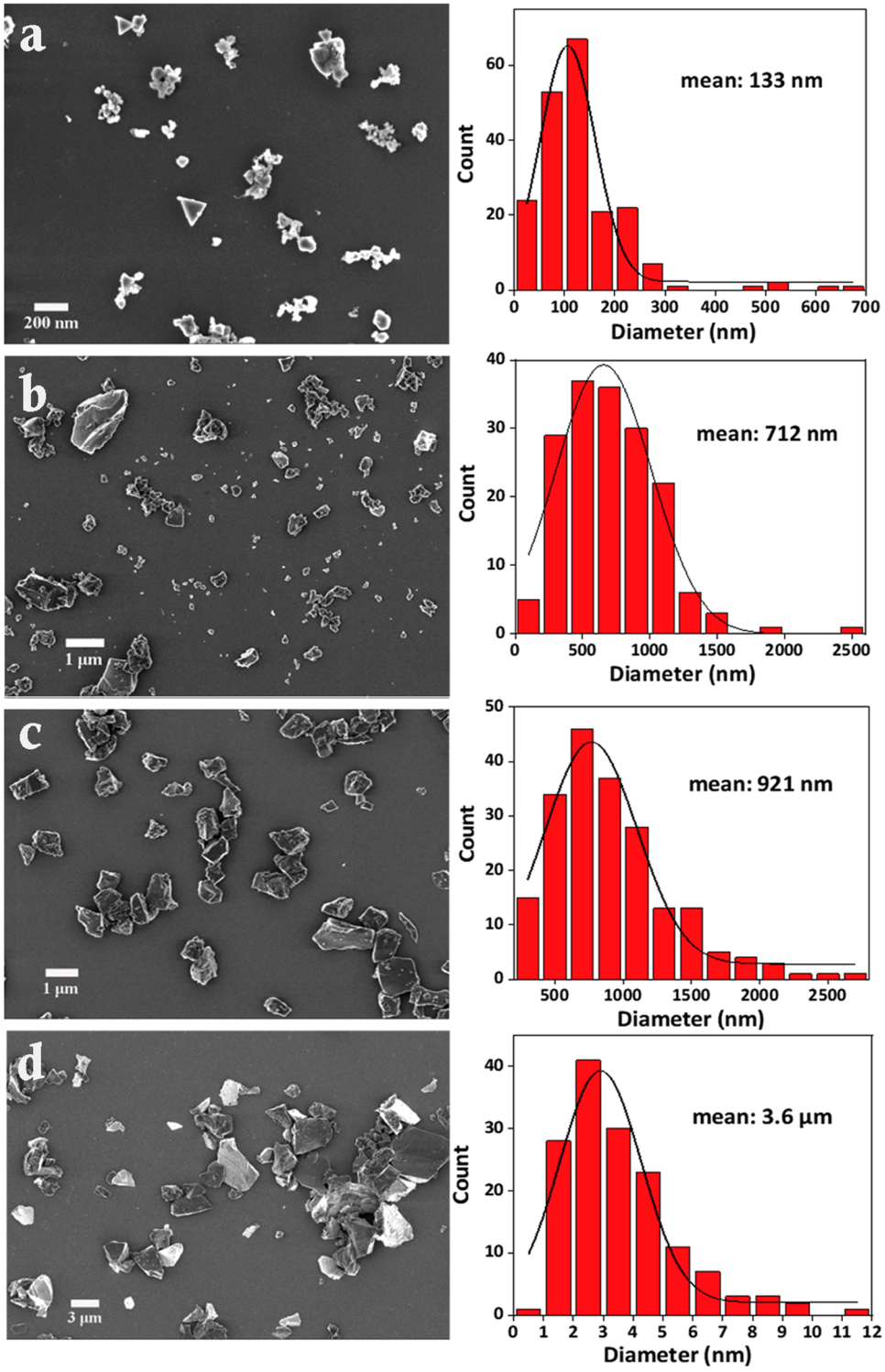

Figure 2. Electron micrographs of representative SiC involving 200 particles in calculation: (a) α-$SiC_{5-250,PC}$, scale bar, 200 nm; (b) α-$SiC_{650,Ab}$, scale bar, 1 μm; (c) α-$SiC_{800,US}$, scale bar, 1 μm; and (d) α-$SiC_{2200,Ab}$, scale bar, 3 μm.

1b), though this sample exhibits only a relatively weak and shifted EPR signal (g-value ~2.0573). All other α-SiC particles, such as α-$SiC_{800,US}$ and α-$SiC_{2200,Ab}$, display only minimal contributions of silicon oxides (see Figure S2), but show significant densities of free electrons, at g-values between 2.0024 and 2.0026 (see Figure 3b). Interestingly, all β-SiC samples display strong silicon oxide signals in FT-IR (Figures 1b and S2), but none of these samples contain satisfactory concentrations of free electrons, similar to α-$SiC_{5-250,PC}$. Therefore, the free electrons in SiC may originate primarily from divacancies in the crystalline sites, rather than from surface defects. These EPR results indicate that α-SiC without an oxide layer has more potential to be hyperpolarized than β-SiC.

Hyperpolarization of ^{29}Si. DNP profiles against microwave spectra were measured relatively fast, by recording the

https://doi.org/10.1021/acsami.1c07156
ACS Appl. Mater. Interfaces 2021, 13, 30835−30843

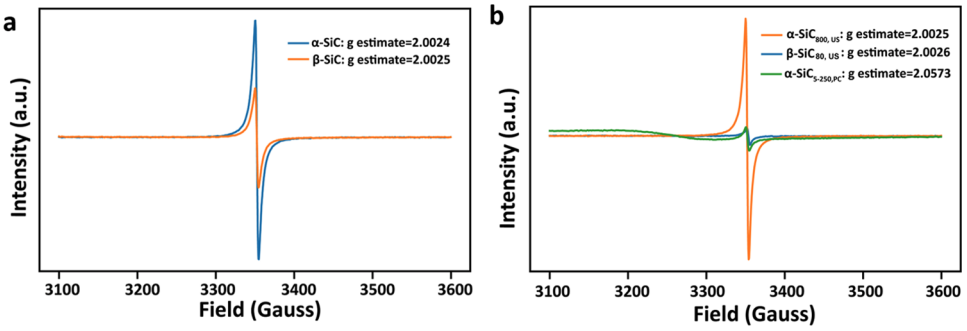

Figure 3. Semiquantitative EPR spectra of (a) α-$SiC_{200-1200,ST}$ and β-$SiC_{100-1200,ST}$ and (b) β-$SiC_{80,US}$, α-$SiC_{5-250,PC}$, α-$SiC_{800,US}$.

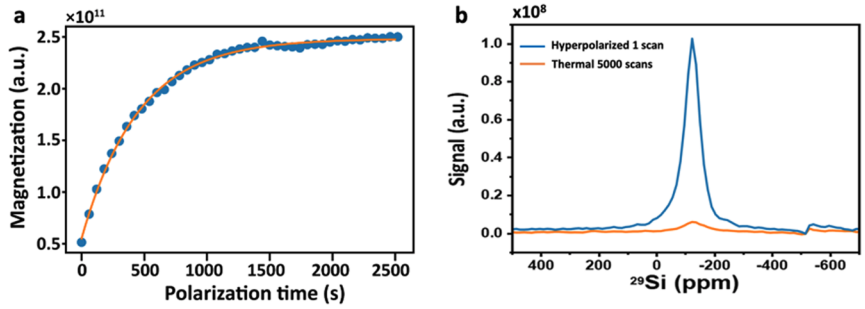

Figure 4. (a) ^{29}Si DNP buildup curve and (b) signal enhancement of α-$SiC_{750,Ab}$ at 4 K.

^{29}Si NMR signal after only 60 s of irradiation (i.e., not after complete polarization). All α-SiC samples, except for α-$SiC_{5-250,PC}$, display obvious DNP signals (see Figure S4). The DNP performance of these α-SiC samples is in good agreement with the aforementioned EPR results, relating high defect densities to strong DNP signals. Figure 4 shows the DNP buildup profile of α-$SiC_{750,Ab}$ with a maximum enhancement of ~34 times at 4 K, by comparing the integrals and correcting for the different flip angle used. Interestingly, the enhanced signal has a narrower linewidth than the thermal signal (1.7 and 2.6 kHz full width at half-maximum, respectively; see Figure S5), which suggests that not all ^{29}Si nuclei in the particle have been polarized. It is, however, also found that all β-SiC samples show poor DNP signals, revealing no significant differences in signal intensities when samples are either hyperpolarized or in thermal equilibrium. Detailed information about SiC samples and their DNP performance can be found in Table S1.

Spin-Lattice Relaxation Times of ^{29}Si. According to previous descriptions of SiC, the source of unpaired electrons in SiC are paramagnetic centers in the lattice.[32] The ^{29}Si nuclei closest to these paramagnetic centers are polarized first, after which transfer of polarization to nuclear spins at further distance occurs through spin diffusion. Therefore, DNP buildup times and T_1 relaxation times may also depend on particle size or rather crystallite size. In addition to the average particle size of each SiC sample, as determined by SEM, the mean crystallite size of each sample was calculated from the XRD data, using the Scherrer equation (see Table S1).[24,46] T_1 relaxation times of α-SiC samples with sufficient DNP signal were recorded at a temperature of 4 K after 1 h of DNP. β-SiC samples and α-$SiC_{5-250,PC}$, which display poor polarization enhancements, are not further investigated. Table 1 summarizes the T_1 relaxation times of the α-SiC samples, demonstrating long T_1 relaxation times, with some samples displaying T_1 times exceeding 20 min, comparable to earlier reported values for similarly sized silicon particles.[19,24,26,29] Larger α-SiC particles, such as α-$SiC_{2200,ABCR}$ with an average particle size of 3.6 μm (from SEM) and a mean crystallite size of 40 nm (from XRD), display considerably longer T_1 times (~22 min) in comparison to smaller particles, such as α-$SiC_{650,ABCR}$ with an average size of 712 nm and a mean crystallite size of 20 nm (T_1 ~ 9 min). T_1 relaxation times and DNP buildup times are not strictly dependent on SiC particle size, as α-$SiC_{800,US}$ is not the largest particle, but does result in the longest T_1 relaxation time of over 26 min.

Table 1. Sample Information and T_1 Relaxation Time of α-SiC Samples

sample	mean size[a]	mean crystallite size (nm)[b]	^{29}Si spin-lattice relaxation time T_1 (s)
α-$SiC_{650,Ab}$	721 nm	20.3	535
α-$SiC_{750,Ab}$	817 nm	28.9	660
α-$SiC_{200-1200,ST}$	755 nm	30.9	961
α-$SiC_{800,US}$	921 nm	27.3	1600
α-$SiC_{2200,Ab}$	3.6 μm	40.2	1315

[a]Mean size as determined by SEM. [b]Mean crystallite size as determined from XRD, using the Scherrer equation.

Hyperpolarization of ^{13}C. Considering the structure of SiC with both covalently bound Si and C atoms, the promising ^{29}Si hyperpolarization results prompted us to also investigate hyperpolarization of the ^{13}C spin species in this material. Based on the ^{29}Si DNP enhancement results, α-$SiC_{750,Ab}$ was selected for this evaluation. As shown in Figure 5a, the polarization of ^{13}C results in a strong signal amplification, in particular when considering the over fourfold lower natural abundance of ^{13}C (1.1%) compared to ^{29}Si (4.7%). The polarization buildup time (Figure 5a) for ^{13}C is approximately 13 min when fitted with a monoexponential buildup curve. However, the buildup curve systematically deviated from the monoexponential fit, suggesting the presence of two or more ^{13}C pools with

https://doi.org/10.1021/acsami.1c07156
ACS Appl. Mater. Interfaces 2021, 13, 30835−30843

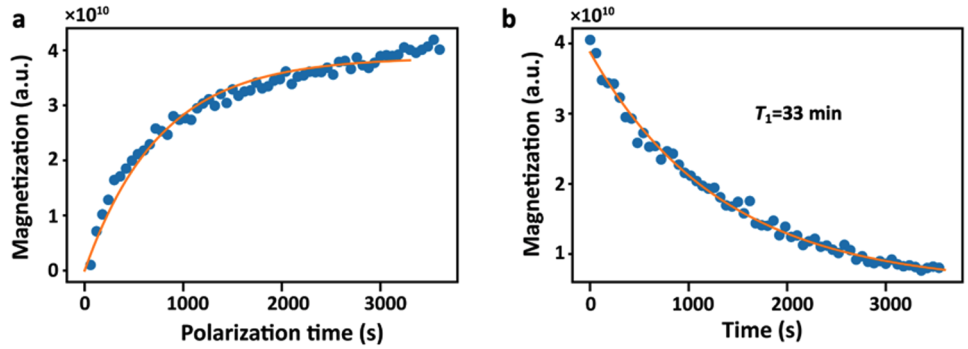

Figure 5. ^{13}C DNP buildup profile (a) and signal sampling during T_1 relaxation (b) of α-$SiC_{750,Ab}$ in the magnetic field of the polarizer (3.38 T).

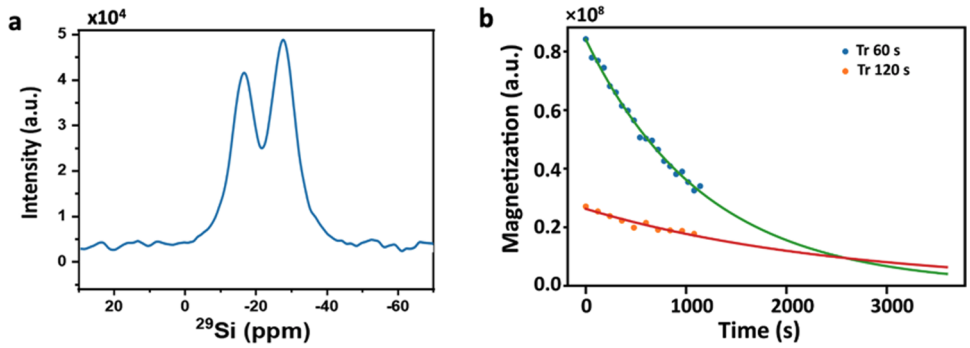

Figure 6. (a) Hyperpolarized ^{29}Si spectra and (b) T_1 fit to the signal decay after DNP of α-$SiC_{750,Ab}$ with two repetition times at 11.7 T.

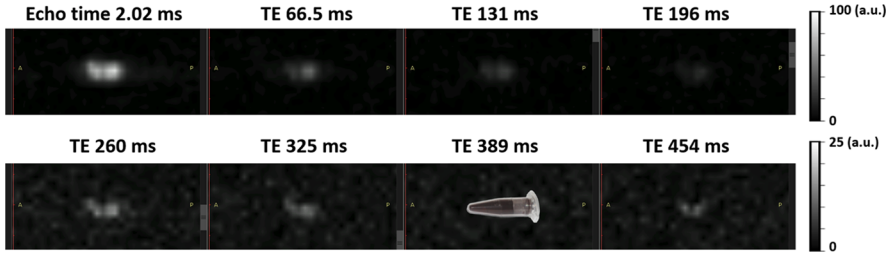

Figure 7. ^{29}Si MR imaging of hyperpolarized α-$SiC_{750,Ab}$ at 11.7 T. Echoes 5−8 are depicted at a fourfold smaller scale to illustrate T_2 signal decay with echo number. In the image of echo 7, the size of the Eppendorf tube is indicated.

different time constants as also reported earlier.[47] Fitting the data with a bi-exponential function provided a better fit, with buildup time constants of 6.5 and 107 min. When after DNP the signal decay was measured with repeated excitations with low flip angle, one single apparent ^{13}C T_1 relaxation time in α-$SiC_{750,Ab}$ of approximately 33 min (Figure 5b) was observed, which was considerably longer than the ^{29}Si T_1 relaxation time of the same particle.

Transfer of α-SiC Samples to 11.7 T. The α-$SiC_{750,Ab}$ sample was selected for transfer to an 11.7 T preclinical MR system. Conventionally, small glassy hyperpolarized molecules with free radicals are dissolved and ejected out of the DNP system with a burst of hot buffer, diluting the solution and increasing the distance between radicals and nuclear spins. Here, our samples could be taken out of the DNP setup as a solid without diluting and transferred to the 11.7 T system in approximately 1 min. For ^{29}Si of α-SiC (6H-SiC polytype) particles the timescale of the relaxation process is independent of temperature and magnetic field.[33] The samples were not actively heated and the temperature was estimated between 100 and 200 K during measurement. Since magnetization typically diminishes rapidly in the absence of a magnetic field, the hyperpolarized SiC nanoparticles were transferred immediately to the 11.7 T MRI system. In a single-shot pulse-acquire spectrum (Figure 6A) at 11.7 T, we observed two ^{29}Si resonances, which were not seen at the low magnetic field (3.38 T) of the polarizer due to a limited spectral resolution and relatively inhomogeneous field. In earlier studies, magic angle spinning NMR spectroscopy on 6H-polytype SiC revealed three ^{29}Si resonances in SiC at 4.7 T at −14, −21, and −25 ppm.[33,48] We only observe two resonances, approximately 11 ppm apart, suggesting that only the two outer resonances of the three are efficiently polarized. This is in agreement with the MAS−NMR-based findings reporting that as soon as any impurities are present, the outer two resonance T_1 times are shorter than the center ^{29}Si peak of 6H-polytype SiC, which can have T_1 times of up to ∼5.5 h at room temperature at 11.7 T.[33] Determining the T_1 relaxation time of this sample is not trivial. Knowing the exact effective flip angle is important to correct the apparent signal decrease for the radiofrequency (RF)-induced decay. Using two experiments at different TR values and an estimated flip angle of 15°, we estimate the T_1 time between 62 and 158 min (Figure 6B). However, as the T_1 time for the two TR settings does not

https://doi.org/10.1021/acsami.1c07156
ACS Appl. Mater. Interfaces 2021, 13, 30835−30843

converge to a single value, nearly all signal decay is governed by the used flip angle, instead of T_1 relaxation. If we only fit a flip angle to these curves, neglecting T_1 relaxation, the fits converge to an effective flip angle between 17.5 and 18.1°. With this actual flip angle and repetition times, we could not properly assess T_1, but can safely assume it is longer than 63 min, the calculated value with a 15° flip and 60 s TR.

MR Imaging. In a separate experiment, the hyperpolarized α-$SiC_{750,Ab}$ sample was transferred to the 11.7 T preclinical MR system to illustrate its potential for imaging the ^{29}Si nuclei. A single slice in sagittal orientation through an Eppendorf tube with the sample produced eight echoes with ^{29}Si signal (Figure 7). The ^{29}Si axial images with six echo times can also be seen in Figure S6.

Fitting monoexponential curves to the signal decay of the center 18 voxels in the multiecho images resulted in an average T_2 relaxation time of 50 ms (SD 13 ms). The multiecho images can be used to calculate a single (weighted) sum image, or after pixel fitting of relaxation decays used to reconstruct images at any given echo time between 0 and approximately 500 ms with improved SNR.

CONCLUSIONS

Hyperpolarization of silicon carbide is demonstrated for micro- and nanoparticles with different crystal phases, particle sizes, and surface groups. α-SiC micro- and nanoparticles show strong DNP signal enhancements due to their high densities of free electrons. In contrast, β-SiC particles consistently showed poor DNP enhancements. Both ^{29}Si and ^{13}C nuclei in α-SiC particles were successfully polarized in the absence of external radicals, revealing long T_1 relaxation times and strong signal amplifications, enabling background-free MR imaging over prolonged periods of time. The Larmor frequencies of ^{29}Si and ^{13}C are both within the tuning ranges of commercial multinuclear MRI systems, greatly facilitating clinical translation. SiC displays high biocompatibility and minimal (cyto)toxicity,[49,50] is chemically inert, and can retain hyperpolarization for several hours, making SiC particles promising for use as high-sensitivity imaging agents for MRI. Further studies are focused on the preparation and selection of uniformly sized SiC nanoparticles, investigation of their biostability and biocompatibility, and modification of their surface with functional groups/ligands for targeted imaging and theranostic applications.

ASSOCIATED CONTENT

Supporting Information

The Supporting Information is available free of charge at https://pubs.acs.org/doi/10.1021/acsami.1c07156.

NMR properties of all SiC samples, XRD diffraction patterns, IR spectra, SEM images, DNP buildup curves, ^{29}Si NMR spectra of hyperpolarized SiC particles and in thermal equilibrium, and ^{29}Si axial imaging of hyperpolarized SiC particles (PDF)

AUTHOR INFORMATION

Corresponding Authors

Tom W. J. Scheenen − *Department of Medical Imaging, Radboud University Medical Center, Nijmegen, 6500 HB Nijmegen, The Netherlands*; Email: Tom.Scheenen@radboudumc.nl

Jos M. J. Paulusse − *Department of Biomolecular Nanotechnology, MESA+ Institute for Nanotechnology, Faculty of Science and Technology, University of Twente, 7500 AE Enschede, The Netherlands; Department of Nuclear Medicine and Molecular Imaging, University Medical Center Groningen, 9700 RB Groningen, The Netherlands;* orcid.org/0000-0003-0697-7202; Email: J.M.J.Paulusse@utwente.nl

Authors

Min Lin − *Department of Biomolecular Nanotechnology, MESA+ Institute for Nanotechnology, Faculty of Science and Technology, University of Twente, 7500 AE Enschede, The Netherlands*

Vincent Breukels − *Department of Medical Imaging, Radboud University Medical Center, Nijmegen, 6500 HB Nijmegen, The Netherlands*

Complete contact information is available at: https://pubs.acs.org/10.1021/acsami.1c07156

Notes

The authors declare no competing financial interest.

ACKNOWLEDGMENTS

The authors gratefully acknowledge funding from the Netherlands Organization for Health Research and Development (ZonMw, project number 435004524). This research was funded by Alzheimer Netherlands and co-funded by the PPP Allowance made available by Health~Holland, Top Sector Life Sciences & Health, to stimulate public−private partnerships, as well as by the Allowance for Top Consortia for Knowledge and Innovation (TKI) made available by the Dutch Ministry of Economic affairs. Financial support from the China Scholarship Council is gratefully acknowledged (predoctoral fellowship 201706990005 to M.L.). The authors thank Mark Smithers for SEM measurements, as well as Rui Xia for XRD measurements and data analysis support.

REFERENCES

(1) Lee, Y. Dissolution Dynamic Nuclear Polarization−Enhanced Magnetic Resonance Spectroscopy and Imaging: Chemical and Biochemical Reactions in Nonequilibrium Conditions. *Appl. Spectrosc. Rev.* **2016**, *51*, 210−226.

(2) Viale, A.; Aime, S. Current Concepts on Hyperpolarized Molecules in MRI. *Curr. Opin. Chem. Biol.* **2010**, *14*, 90−96.

(3) Barker, P. B.; Lin, D. D. M. In Vivo Proton MR Spectroscopy of the Human Brain. *Prog. Nucl. Magn. Reson. Spectrosc.* **2006**, *49*, 99−128.

(4) Lee, N.; Hyeon, T. Designed Synthesis of Uniformly Sized Iron Oxide Nanoparticles for Efficient Magnetic Resonance Imaging Contrast Agents. *Chem. Soc. Rev.* **2012**, *41*, 2575−2589.

(5) Estelrich, J.; Sanchez-Martin, M. J.; Busquets, M. A. Nanoparticles in Magnetic Resonance Imaging: from Simple to Dual Contrast Agents. *Int. J. Nanomed.* **2015**, *10*, 1727−1741.

(6) Ramalho, J.; Semelka, R. C.; Ramalho, M.; Nunes, R. H.; AlObaidy, M.; Castillo, M. Gadolinium-Based Contrast Agent Accumulation and Toxicity: An Update. *Am. J. Neuroradiol.* **2016**, *37*, 1192−1198.

(7) McDonald, R. J.; McDonald, J. S.; Kallmes, D. F.; Jentoft, M. E.; Murray, D. L.; Thielen, K. R.; Williamson, E. E.; Eckel, L. J. Intracranial Gadolinium Deposition after Contrast-Enhanced MR Imaging. *Radiology* **2015**, *275*, 772−782.

(8) Månsson, S.; Johansson, E.; Magnusson, P.; Chai, C. M.; Hansson, G.; Petersson, J. S.; Stahlberg, F.; Golman, K. 13C Imaging-A new Diagnostic Platform. *Eur. Radiol.* **2006**, *16*, 57−67.

(9) Utsumi, H.; Yamada, K.-i.; Ichikawa, K.; Sakai, K.; Kinoshita, Y.; Matsumoto, S.; Nagai, M. Simultaneous Molecular Imaging of Redox Reactions Monitored by Overhauser-Enhanced MRI with 14N-and 15N-Labeled Nitroxyl radicals. *Proc. Natl. Acad. Sci. U.S.A.* **2006**, *103*, 1463−1468.
(10) Amiri, H.; Srinivas, M.; Veltien, A.; van Uden, M. J.; de Vries, I. J.; Heerschap, A. Cell Tracking Using (19)F Magnetic Resonance Imaging: Technical Aspects and Challenges Towards Clinical Applications. *Eur. Radiol.* **2015**, *25*, 726−735.
(11) Halse, M. E. Perspectives for Hyperpolarisation in Compact NMR. *TrAC, Trends Anal. Chem.* **2016**, *83*, 76−83.
(12) Brindle, K. M.; Bohndiek, S. E.; Gallagher, F. A.; Kettunen, M. I. Tumor Imaging Using Hyperpolarized 13C Magnetic Resonance Spectroscopy. *Magn. Reson. Med.* **2011**, *66*, 505−519.
(13) Brindle, K. M. Imaging Metabolism with Hyperpolarized (13)C-Labeled Cell Substrates. *J. Am. Chem. Soc.* **2015**, *137*, 6418−6427.
(14) van Heijster, F. H.; Heskamp, S.; Breukels, V.; Veltien, A.; Franssen, G. M.; Jansen, K. F.; Boerman, O. C.; Schalken, J. A.; Scheenen, T. W.; Heerschap, A. Pyruvate-Lactate Exchange and Glucose Uptake in Human Prostate Cancer Cell Models. A Study in Xenografts and Suspensions by Hyperpolarized [1-13C] Pyruvate MRS and [18F] FDG-PET. *NMR Biomed.* **2020**, *33*, No. e4362.
(15) Nelson, S. J.; Kurhanewicz, J.; Vigneron, D. B.; Larson, P. E.; Harzstark, A. L.; Ferrone, M.; Van Criekinge, M.; Chang, J. W.; Bok, R.; Park, I.; et al. Metabolic Imaging of Patients with Prostate Cancer using Hyperpolarized [1-13C] Pyruvate. *Sci. Transl. Med.* **2013**, *5*, No. 198ra108.
(16) Keshari, K. R.; Wilson, D. M. Chemistry and Biochemistry of 13C Hyperpolarized Magnetic Resonance Using Dynamic Nuclear Polarization. *Chem. Soc. Rev.* **2014**, *43*, 1627−1659.
(17) Hoch, M. J.; Reynhardt, E. C. Nuclear Spin-Lattice Relaxation of Dilute Spins in Semiconducting Diamond. *Phys. Rev. B* **1988**, *37*, 9222−9226.
(18) Bretschneider, C. O.; Akbey, Ü.; Aussenac, F.; Olsen, G. L.; Feintuch, A.; Oschkinat, H.; Frydman, L. On the Potential of Dynamic Nuclear Polarization Enhanced Diamonds in Solid-State and Dissolution 13C NMR Spectroscopy. *ChemPhysChem* **2016**, *17*, 2611.
(19) Aptekar, J. W.; Cassidy, M. C.; Johnson, A. C.; Barton, R. A.; Lee, M.; Ogier, A. C.; Vo, C.; Anahtar, M. N.; Ren, Y.; Bhatia, S. N.; et al. Silicon Nanoparticles as Hyperpolarized Magnetic Resonance Imaging Agents. *ACS Nano* **2009**, *3*, 4003−4008.
(20) Dutta, P.; Martinez, G. V.; Gillies, R. J. Nanodiamond as a New Hyperpolarizing Agent and Its (13)C MRS. *J. Phys. Chem. Lett.* **2014**, *5*, 597−600.
(21) Whiting, N.; Hu, J.; Shah, J. V.; Cassidy, M. C.; Cressman, E.; Millward, N. Z.; Menter, D. G.; Marcus, C. M.; Bhattacharya, P. K. Real-time MRI-guided Catheter Tracking using Hyperpolarized Silicon particles. *Sci. Rep.* **2015**, *5*, No. 12842.
(22) Rej, E.; Gaebel, T.; Boele, T.; Waddington, D. E.; Reilly, D. J. Hyperpolarized Nanodiamond with Long Spin-Relaxation Times. *Nat. Commun.* **2015**, *6*, No. 8459.
(23) Cassidy, M. C.; Chan, H. R.; Ross, B. D.; Bhattacharya, P. K.; Marcus, C. M. In Vivo Magnetic Resonance Imaging of Hyperpolarized Silicon Particles. *Nat. Nanotechnol.* **2013**, *8*, 363−368.
(24) Kwiatkowski, G.; Polyhach, Y.; Jähnig, F.; Shiroka, T.; Starsich, F. H.; Ernst, M.; Kozerke, S. Exploiting Endogenous Surface Defects for Dynamic Nuclear Polarization of Silicon Micro-and Nanoparticles. *J. Phys. Chem. C* **2018**, *122*, 25668−25680.
(25) Lafon, O.; Thankamony, A. S. L.; Rosay, M.; Aussenac, F.; Lu, X.; Trébosc, J.; Bout-Roumazeilles, V.; Vezin, H.; Amoureux, J.-P. Indirect and Direct 29Si Dynamic Nuclear Polarization of Dispersed Nanoparticles. *Chem. Commun.* **2013**, *49*, 2864−2866.
(26) Whiting, N.; Hu, J.; Zacharias, N. M.; Lokesh, G. L.; Volk, D. E.; Menter, D. G.; Rupaimoole, R.; Previs, R.; Sood, A. K.; Bhattacharya, P. Developing Hyperpolarized Silicon Particles for In Vivo MRI Targeting of Ovarian Cancer. *J. Med. Imaging* **2016**, *3*, No. 036001.
(27) Atkins, T. M.; Cassidy, M. C.; Lee, M.; Ganguly, S.; Marcus, C. M.; Kauzlarich, S. M. Synthesis of Long T1 Silicon Nanoparticles for Hyperpolarized 29Si Magnetic Resonance Imaging. *ACS Nano* **2013**, *7*, 1609−1617.
(28) Seo, H.; Choi, I.; Whiting, N.; Hu, J.; Luu, Q. S.; Pudakalakatti, S.; McCowan, C.; Kim, Y.; Zacharias, N.; Lee, S.; Bhattacharya, P.; Lee, Y. Hyperpolarized Porous Silicon Nanoparticles: Potential Theragnostic Material for 29Si Magnetic Resonance Imaging. *ChemPhysChem* **2018**, *19*, 2143−2147.
(29) Kwiatkowski, G.; Jahnig, F.; Steinhauser, J.; Wespi, P.; Ernst, M.; Kozerke, S. Nanometer Size Silicon Particles for Hyperpolarized MRI. *Sci. Rep.* **2017**, *7*, No. 7946.
(30) Saddow, S. E. *Silicon Carbide Biotechnology: A Biocompatible Semiconductor for Advanced Biomedical Devices and Applications*; Elsevier, 2012.
(31) Falk, A. L.; Klimov, P. V.; Ivády, V.; Szász, K.; Christle, D. J.; Koehl, W. F.; Gali, Á.; Awschalom, D. D. Optical Polarization of Nuclear Spins in Silicon Carbide. *Phys. Rev. Lett.* **2015**, *114*, No. 247603.
(32) Ivády, V.; Szász, K.; Falk, A. L.; Klimov, P. V.; Christle, D. J.; Janzén, E.; Abrikosov, I. A.; Awschalom, D. D.; Gali, A. Theoretical Model of Dynamic Spin Polarization of Nuclei Coupled to Paramagnetic Point Defects in Diamond and Silicon Carbide. *Phys. Rev. B* **2015**, *92*, No. 115206.
(33) Hartman, J. S.; Narayanan, A.; Wang, Y. Spin-Lattice Relaxation in the 6H Polytype of Silicon Carbide. *J. Am. Chem. Soc.* **1994**, *116*, 4019−4027.
(34) Comment, A.; van den Brandt, B. V.; Uffmann, K.; Kurdzesau, F.; Jannin, S.; Konter, J.; Hautle, P.; Wenckebach, W. T.; Gruetter, R.; Van Der Klink, J. Design and Performance of a DNP Prepolarizer Coupled to a Rodent MRI Scanner. *Concepts Magn. Reson., Part B: Magn. Reson. Eng.* **2007**, *31B*, 255−269.
(35) van Meerten, S.; Franssen, W.; Kentgens, A. ssNake: A Cross-Platform Open-Source NMR Data Processing and Fitting Application. *J. Magn. Reson.* **2019**, *301*, 56−66.
(36) Iwanowski, R.; Fronc, K.; Paszkowicz, W.; Heinonen, M. XPS and XRD Study of Crystalline 3C-SiC Grown by Sublimation Method. *J. Alloys Compd.* **1999**, *286*, 143−147.
(37) Toprak, M. S.; Nikkam, N.; Saleemi, M.; Haghighi, E. B.; Ghanbarpour, M.; Khodabandeh, R.; Muhammed, M.; Palm, B. Fabrication, Characterization and Thermo-Physical Property Evaluation of SiC Nanofluids for Heat Transfer Applications. *Nano-Micro Lett.* **2014**, *6*, 178−189.
(38) Gorthy, P. Production of Silicon Carbide from Rice Husks. *J. Am. Ceram. Soc.* **1999**, *82*, 1393−1400.
(39) Xu, T. T.; Cheng, S.; Jin, L. Z.; Zhang, K.; Zeng, T. High-Temperature Flexural Strength of SiC Ceramics Prepared by Additive Manufacturing. *Int. J. Appl. Ceram. Technol.* **2020**, *17*, 438−448.
(40) Oliveros, A.; Guiseppi-Elie, A.; Saddow, S. E. Silicon Carbide: a Versatile Material for Biosensor Applications. *Biomed. Microdevices* **2013**, *15*, 353−368.
(41) Camassel, J.; Juillaguet, S.; Zielinski, M.; Balloud, C. Application of LTPL Investigation Methods to CVD-Grown SiC. *Chem. Vap. Deposition* **2006**, *12*, 549−556.
(42) Li, Y.; Chen, C.; Li, J.-T.; Yang, Y.; Lin, Z.-M. Surface Charges and Optical Characteristic of Colloidal Cubic SiC Nanocrystals. *Nanoscale Res. Lett.* **2011**, *6*, No. 454.
(43) Merle-Méjean, T.; Abdelmounm, E.; Quintard, P. Oxide Layer on Silicon Carbide Powder: a FT-IR Investigation. *J. Mol. Struct.* **1995**, *349*, 105−108.
(44) Macfarlane, P.; Zvanut, M. Generation and Annealing Characteristics of Paramagnetic Centers in Oxidized 3C-SiC and 6H-SiC. *J. Electron. Mater.* **1999**, *28*, 144−147.
(45) von Bardeleben, H.; Rauls, E.; Gerstmann, U. Carbon Vacancy-Related Centers in 3 C-Silicon Carbide: Negative-U Properties and Structural Transformation. *Phys. Rev. B* **2020**, *101*, No. 184108.
(46) Yushin, G. N.; Hoffman, E. N.; Nikitin, A.; Ye, H.; Barsoum, M. W.; Gogotsi, Y. Synthesis of Nanoporous Carbide-Derived Carbon by

Chlorination of Titanium Silicon Carbide. *Carbon* **2005**, *43*, 2075−2082.
(47) Richardson, M. F.; Hartman, J. S.; Guo, D.; Winsborrow, B. G. NMR Chemical Shift Tensors and Peak Assignments for the 6H Polytype of Silicon Carbide. *Chem. Mater.* **1992**, *4*, 318−323.
(48) Hartman, J. S.; Richardson, M. F.; Sherriff, B. L.; Winsborrow, B. G. Magic Angle Spinning NMR Studies of Silicon Carbide: Polytypes, Impurities, and Highly Inefficient Spin-Lattice Relaxation. *J. Am. Chem. Soc.* **1987**, *109*, 6059−6067.
(49) Fan, J.; Chu, P. K. Group IV Nanoparticles: Synthesis, Properties, and Biological Applications. *Small* **2010**, *6*, 2080−2098.
(50) Yakimova, R.; Petoral, R., Jr.; Yazdi, G.; Vahlberg, C.; Spetz, A. L.; Uvdal, K. Surface Functionalization and Biomedical Applications Based on SiC. *J. Phys. D: Appl. Phys.* **2007**, *40*, 6435.

https://doi.org/10.1021/acsami.1c07156
ACS Appl. Mater. Interfaces 2021, 13, 30835−30843